SMALL BODIES IR IMAGING FOR VISION BASED RELATIVE NAVIGATION AND MAPPING ENHANCEMENT

G.L. Civardi[a,1,*], M. Piccinin[a,2,*], M. Lavagna[a,3,*]

[a]Department of Aerospace Science and Technology, Politecnico di Milano, Milano, Italy

Abstract

This work investigates the potentialities of multispectral imaging data fusion for relative navigation, mapping and dynamical characterization of an unknown celestial body. A vision-based navigation algorithm is designed to work on both visible (VIS) and thermal infrared (TIR) images, with the aim of estimating the spacecraft's relative pose while reconstructing the target's shape. The output of the Image Processing (IP) is then considered as the primary measurement source for an Extended Kalman Filter (EKF), that fuses camera output with inertial measurements to refine the pose estimate and reconstruct the asteroid's spin state. Experimental results suggest that the proposed data fusion approach can effectively enhance the navigation solution accuracy without requiring any additional on-board hardware complexity.

Keywords: Asteroids missions, Relative navigation, Multispectral image processing, Spin state characterization, Simultaneous Localization And Mapping

1. Introduction

Small celestial bodies represent some of the principal targets of exploration missions in the last decades. The subset of Near Earth Objects (NEO) family, which are candidates for Earth impacting, currently constitute the main target of on-going activities and research for planetary defense [1]. Missions towards small celestial bodies have to deal with a harsh and partially unknown environment, together with operational challenges such as telecommunication delays. The probe is typically asked to orbit close to a small object, unknown in shape and dynamics, to progressively characterize it in terms of geophysical and dynamical properties. To this aim, different technologies are embarked, among which multispectral imaging sensors play a fundamental role to support both body shape and thermophysical properties reconstruction. Images collected by the visible (VIS) camera are processed on ground using stereophotoinclinometry and stereophotogrammetry techniques to reconstruct the object's shape [2],[3], while thermal infrared (TIR) images provide information regarding the thermophysical properties [4], useful to reconstruct an hazard map. The combination of this information can be exploited to select a safe landing site for the probe, leveraging knowledge about the body's topology and composition. Besides scientific investigation, imaging data are also a powerful tool for relative Guidance, Navigation and Control (GNC) purposes. Visible on-board cameras are nowadays employed for centroiding techniques during approach and early characterization phases, while a landmark-based navigation solution is employed during proximity operations, as recently demonstrated by NASA's OSIRISREx [5]. Despite the widespread use of thermal imaging for scientific applications, GNC operations are still entrusted to

---

*Corresponding author

Email addresses: `gaialetizia.civardi@mail.polimi.it` (G.L. Civardi), `margherita.piccinin@polimi.it` (M. Piccinin), `michelle.lavagna@polimi.it` (M. Lavagna)

[1]Master Student, Department of Aerospace Science and Technology, Politecnico di Milano
[2]PhD Candidate, Department of Aerospace Science and Technology, Politecnico di Milano
[3]Full Professor, Department of Aerospace Science and Technology, Politecnico di Milano

optical imaging only. The first attempt of introducing thermal imaging for navigation purposes is represented by the Hayabusa-2 mission. The onboard Thermal Infrared Imager (TIR) contributed to the mission success allowing to detect the deployable artifical markers against the sun-lit asteroid face, which made it possible to perform an autonomous landing operation [6]. Considering these capabilities, thermal imaging can be regarded as a potentially useful and applicable tool to support GNC tasks, as hypothesized in [7]. Multispectral data fusion increases the reliability of the navigation scheme in case of shadows and high Sun phase angle, while the combination of shape and temperature information allows a deeper and faster understanding of the asteroid's composition and inertia reconstruction towards its spin history identification. This work seeks to investigate the potential benefits of including the already onboard thermal imager in the navigation chain. A stand-alone vision-based navigation and mapping algorithm relying on a mono-camera as the main sensor has been developed to work on both the visible and the thermal infrared spectrum. Synthetic images have been generated on purpose to benchmark the algorithm's performances, proposing a simple domain translation methodology to obtain thermal infrared images without the need of a dedicated rendering software. A navigation filter for relative pose estimation and spin state characterization has been developed to work in combination with the Image Processing (IP) output. Performance assessment of the two main components of the navigation chain is then presented, highlighting the benefits of multispectral data fusion in terms of navigation solution accuracy.

This paper is organized as follows: in Section 2 synthetic images rendering is addressed; in Section 3 the Vision Based navigation algorithm is presented and its performances are critically analyzed. In Section 4 the relative navigation filter is described and performances of an extensive Montecarlo simulation are reported. To conclude, the key findings are summarized and discussed in Section 5, together with some hints for future studies.

2. Synthetic TIR images rendering

Visible images are obtained using PANGU [8]. Concerning thermal infrared images, since dedicated rendering tools are still under development, a simple domain translation methodology is here proposed. The starting point for the generation of synthetic TIR frames is represented by the available rendering software and the asteroid's thermal model. Two different thermal models are compared to identify the application range of the proposed domain translation methodology. The models are here listed with increasing complexity.

Simplified thermal model. The simplest thermal model stems from the idea that the thermal emission from any point on an asteroid's surface can be considered to be in instantaneous equilibrium with the solar radiation absorbed at that point, as proposed in [9]. The equilibrium condition is formalized as:

$$Q_{in} = Q_{out} \tag{1}$$

In which Q_{in} is the heating solar flux, while Q_{out} the thermal emission from the asteroid. The solar flux is a function depending on the distance with respect to the Sun and on the incidence angle ϕ between the direction of the Sun and the normal vector to the heated surface:

$$Q_{in} = S_\odot (1 - A) \left(\frac{AU}{r}\right)^2 \cos(\phi) \tag{2}$$

where $S_\odot$ is the solar constant and A is the bolometric Bond albedo. The flux emitted by the asteroid at the thermal equilibrium is written as:

$$Q_{out} = \epsilon \sigma u^4 \tag{3}$$

in which ϵ is the emissivity of the surface of the asteroid, u is the temperature of the asteroid and σ is the Stefan-Boltzman constant. Within this context, the equilibrium temperature of the body is expressed as:

$$u = \left(\frac{S_\odot (1 - A)}{\epsilon \sigma} \left(\frac{AU}{r}\right)^2 \cos(\phi)\right)^{1/4} = u_0 \cos(\phi)^{1/4} \tag{4}$$

In which the *subsolar temperature* u_0 is obtained for $\phi = 0$. The temperature distribution over the body is then only described through the solar incidence angle. The temperature on the nightside of the asteroid $\phi \geq 90°$ is assumed to be zero, which is a reasonable assumption at small Sun Phase Angles (SPA) where the dayside flux dominates. However, since a thermal camera is especially useful to provide information for high SPA, it is essential to introduce a more complex model.

Complete thermal model. A more realistic thermal model should take into account that the asteroid's dark side is progressively cooling down and that a certain amount of the Sun heat flux is stored in the ground layers. To model these phenomena, it is necessary to introduce a temporal dependency for the temperature profile, in such way that also the spin state can be accounted for. Furthermore, thermal conduction must be considered at least in the radial direction, to include the contribution of different ground layers. The basic equation underlying this thermal model is the following:

$$Q_{in} = Q_{out} + Q_s \tag{5}$$

In which Q_s represents the heat flux at the surface of the asteroid. This heat flux at the surface of the asteroid is linked to the 1D temperature gradient:

$$Q_s = -k \left.\frac{\partial u}{\partial x}\right|_{x=0} \tag{6}$$

Where k is the conductivity of the asteroid, and the x coordinate is taken in the radial direction, positive downwards. To model the heat transfer in the ground, it is necessary to use the heat conduction equation, in which a constant conductivity is assumed for simplicity:

$$\rho c_p \frac{\partial u(t, x)}{\partial t} = k \frac{\partial u(t, x)}{\partial x^2} \tag{7}$$

Where ρ is the density and c_p the specific heat capacity. More parameters are necessary to describe the properties of asteroid, namely the thermal inertia Γ and the annual thermal skin depth l_s:

$$\Gamma = \sqrt{k\rho c_p} \qquad l_s = \sqrt{\alpha \pi p} \tag{8}$$

Where p is the orbital period of the asteroid and the diffusivity α defines the material property. The thermal inertia quantifies the ability of the material to keep its actual temperature. The higher the thermal inertia is, the smoother the temperature variation will be. The skin depth is regarded as the depth of the ground where an adiabatic assumption can be acceptable, which means a null heat flux. Finally, boundary conditions are set to complete the model of Eq. (7)

$$\begin{cases} u(0, x) = f(x) & \forall\ x \in [0, l_s] \\ u_x(0, t) = \frac{Q_{out} - Q_{in}}{k} & \forall\ t \geq 0 \\ u_x(l_s, t) = 0 & \forall\ t \geq 0 \end{cases} \tag{9}$$

Where u_x denotes the partial derivative of temperature with respect to the spatial coordinate x. Details regarding the model validation and discussion are available in [10] and [11], while only some key results are here reported.

Within this framework, due to its relevance to the upcoming HERA project [12], Didymos has been selected as the target of our simulations. Since no detailed thermophysical characterization of Didymos and its moon Dimorphos is available, the material properties were chosen considering ESA's reference model [13], while the thermal inertia was set to an intermediate value of $\Gamma = 500\ Jm^{-2}K^{-1}s^{-0.5}$, building on past missions collected data. In this simplified simulation the obliquity δ was neglected, and since Didymos' orbit about the Sun is only inclined of 3° about the ecliptic, the asteroid's inclination has been neglected as well. Notice that a constant angular velocity about the asteroid's z–axis has been assumed. Even though the real spin state is more complex, the model can be still considered as representative of the thermal behaviour. The temperature distribution is then evaluated ad a distance of 1.6 AU, using both models. Results are reported in Fig. 1. The temperature range of the sunlit face of the asteroid is similar in the two cases, with only a small difference of about $25\ K$. As expected, the complete thermal model reported in Fig. 1b can correctly describe the temperature gradient between the dayside and the nightside of the asteroid. Since Didymain's rotation period about its spin axis is only $2.26\ hrs$, the temperature distribution is smooth, as the dark side cannot cool down significantly.

3

Figure 1: Thermal model comparison

**(a) Simple model**

(b) Complete model
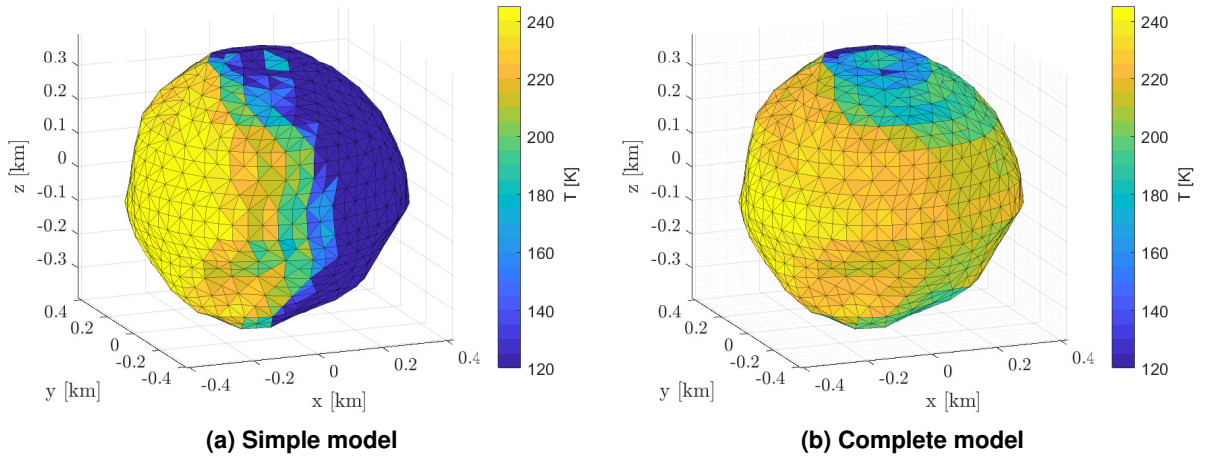
TIR images generation. From the comparison of the thermal models, it can be concluded that the simple thermal model can still provide a truthful temperature description for small SPA. If the simplified thermal model holds true, considering uniform physical properties, the temperature only depends on local Sun incidence angle. This information is not directly available from imaging data, yet it can be empirically related to the observed punctual brightness. Considering Eq. (4), the information related to the Sun incidence angle is replaced by the single pixel brightness. The results still match the overall minimum and maximum temperature expected at the asteroid's surface, while further improvements need to be introduced to generate a meaningful temperature spatial distribution. A further step towards a more realistic rendering is represented by the generation of a synthetic emissivity map, whose aim is to simulate an heterogeneous material distribution that reacts differently when illuminated. It can be then concluded that the proposed methodology is only applicable for low SPA and for simple shapes, where self-shadowing is not present. Nevertheless, this approach is still useful for a preliminary performance assessment of IP algorithms. An example of two frames in the different sensing modalities is presented in Fig. 2, considering a spheroidal shape for Didymos rendering. Selected camera parameters are reported in Table 1.

Table 1: VIS and TIR camera parameters

	FOV [deg]	**Sensor Size** $[px^2]$
VIS cam	11×11	1024×1024
TIR cam	11×11	512×512

4

Figure 2: Synthetic VIS (left) and TIR (right) images

(a) Synthetic visible image

(b) Synthetic thermal infrared image
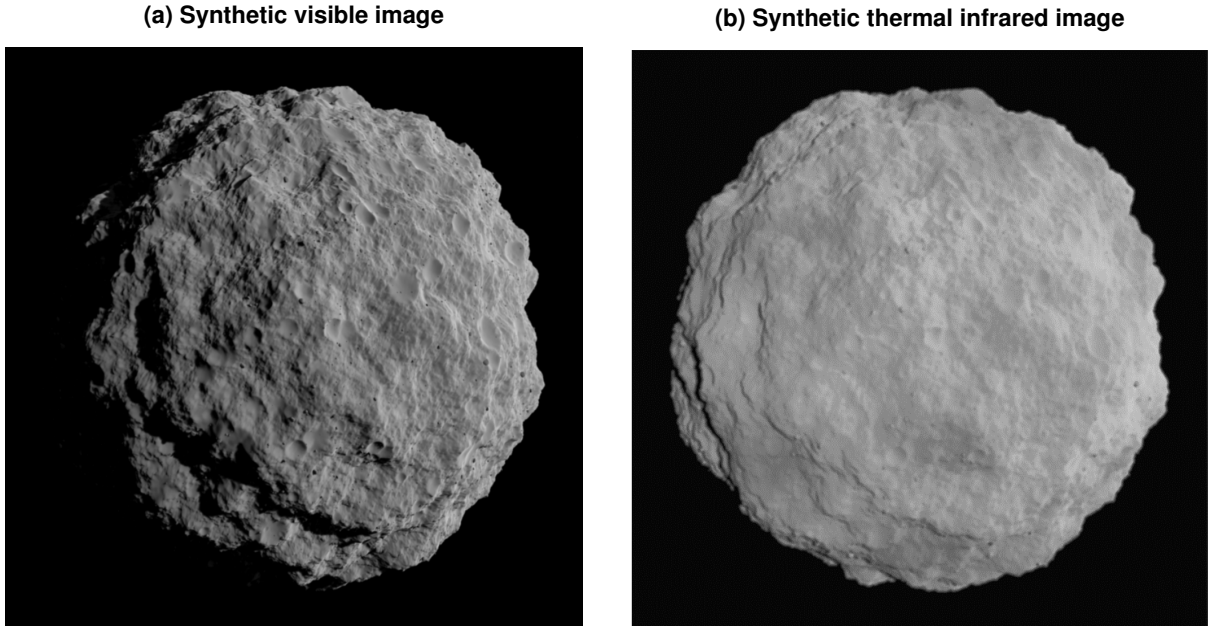
3. Image processing algorithm

The implemented vision-based navigation algorithm relies on the incoming images and does not require any previous knowledge regarding the target's geometry. Hereafter, all the main building blocks are described together with details regarding the implementation choices. Results of a preliminary testing campaing are also reported, highlighting the differences between the two available sensing modalities.

3.1. Algorithm description

The developed vision-based navigation algorithm builds on concepts of Visual Odometry (VO) and Visual-SLAM (V-SLAM). The pipeline is capable of working in both the visible and the thermal infrared spectrum. Features are extracted and tracked from the incoming image stream, while at the same time a sparse 3D map of the asteroid is reconstructed and used for navigation. The relative position and attitude of the probe are optimized using Bundle Adjustment (BA) [14], that is a widely used technique in the computer vision field. A schematic outline of the algorithm is presented in Fig. 3, while a brief summary is here presented.

Figure 3: V-SLAM algorithm
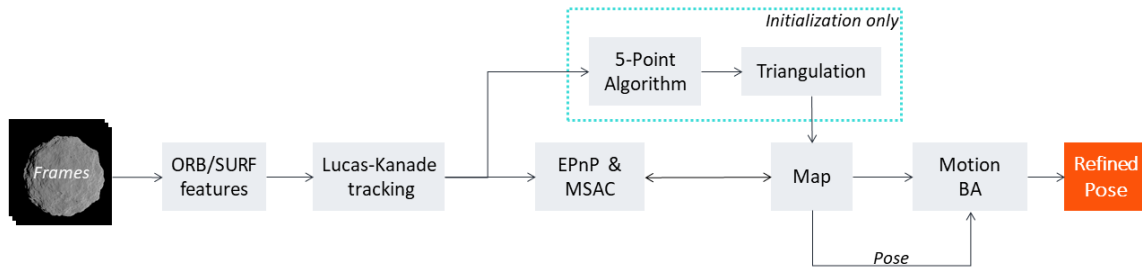
Feature detection. A *feature* or *keypoint* is defined as a point of interest in an image, usually in the form of corners, blobs and lines. Among all the different feature extraction approaches, Oriented FAST and Rotated BRIEF (ORB) [15] is exploited for VIS images, while Speeded-up Robust Features (SURF) [16] is employed for TIR images. To further improve the spatial keypoint distribution over the image, adaptive non-maximal suppression (ANMS) with suppression via square covering (SSC) is employed [17], that is able to enforce a better spatial distribution by jointly taking into account the keypoints strength and their localization. An upper bound of 400 features is set to constrain the computational burden.

Feature tracking. Features are extracted from the first frame and are then tracked on the subsequent images using the pyramidal Lucas-Kanade algorithm [18]. After the tracking process, a keypoint culling procedure is implemented to discard features that have been erroneously tracked or the ones tracked with low accuracy. The number of tracked features tends to decrease as the trajectory develops, therefore new keypoints must be initialized. New features are merged with the old ones that are still being tracked at the time of re-detection, provided that they are sufficiently distant.

Motion Estimation. In the main V-SLAM module, motion estimation relies on correspondences between 2D tracked features and 3D map points. For this reason, the map must be built and initialized to boot-strap the algorithm. In the initialization module, keypoints detected in the first frame are tracked from the first frame through all intermediate frames up to the actual second initialization frame. The essential matrix is estimated through the 5-point algorithm [19], that is nested within an MSAC [20] routine for robustness purposes. The essential matrix is then decomposed using Singular Value Decomposition (SVD), obtaining a rotation matrix and a translation vector (up to scale). Landmarks can be now triangu-lated using the relative pose information. Once the 3D sparse map is initialized and the 2D features are tracked, for each incoming image a set of 3D to 2D map to features correspondences is retrieved and used to solve the *Perspective-n-Point problem* (PnP). P3P [21] and EPnP [22] algorithms are exploited to this aim. The P3P algorithm is combined with MSAC in order to remove outliers from the initial set of correspondences. The resulting set of Map-To-Frame correspondences is then fed to the EPnP solver, that is a non-iterative solution of the problem and is applicable both for planar and non planar map point configurations. The last step is represented by a Gauss-Newton iterative optimization, which further refines the EPnP pose estimate.

Mapping. When the map is first initialized, badly triangulated landmarks must be pruned to preserve localization performances. Landmarks must have a positive z coordinate in the current camera frame, which means that they are actually in front of the camera and visible. Furthermore, an upper limit on the distance from the camera is imposed, since far away points tend to have a higher uncertainty. This limitation is practically implemented by imposing a threshold on the ratio between the maximum z co-ordinate and the median of the depth of the landmarks. Each time new keypoints are initialized, an attempt of triangulation is made, using the previously stored pose information. To make sure that the newly added landmarks respect some quality standards, the angle between the between the bearing vectors corresponding to the keypoints observations and camera poses must be greater than a prede-fined value. In addition, the reprojection error of the candidate landmarks must not exceed a defined error threshold. In this way wrong feature tracks resulting in skew bearing vectors are removed.

Optimization. Motion estimation is an error prone step and it does not have sufficient accuracy in trajec-tory reconstruction by itself. Besides, motion is reconstructed in an incremental way, which means that error tends to build up and exponentially grow as the trajectory develops. This results in an increasing drift in time which is classical of any VO or V-SLAM problems. To prevent the motion estimation error from accumulating, BA is implemented, exploiting the Sparse Bundle Adjustment (SBA) software pack-age [23] available in MATLAB environment. To reduce the computational load of the algorithm, Motion Only BA is performed, meaning that only the pose is optimized, keeping the 3D landmark coordinates fixed.

3.2. Simulations and results

The synthetic images used as benchmark have been obtained using PANGU, adopting the previously described domain translation methodology and camera parameters (Table 1). Considering a trade-off between real hardware capabilities and image processing performances, it is assumed that a picture is taken every 30 s approximately. This frame rate is used in combination with Didymos revolution period to generate a realistic image sequence. Results are here presented for a long sequence of 300 frames, which in turn translates into a complete revolution around the asteroid, considering the asteroid fixed frame. A simple circular trajectory was selected, with a radius of approximately 5 km and an inclination of 20°. An overview of the ground truth trajectory and the reconstructed one is reported in Fig. 4 for both sensing modalities. Please notice that the motion is reconstructed up to scale, and that trajectory alignment and scaling are performed in the post-processing phase.
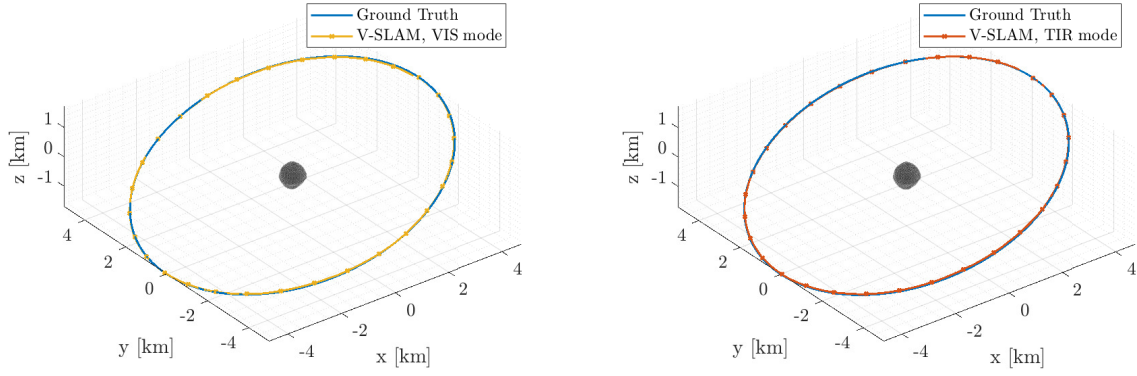
(a) Reconstructed trajectory, VIS mode

(b) Reconstructed trajectory, TIR mode

Figure 4: Trajectory reconstruction

To evaluate the navigation algorithm performances, the overall position error is computed as:

$$e_\rho = \sqrt{(x_i - \hat{x}_i)^2 + (y_i - \hat{y}_i)^2 + (z_i - \hat{z}_i)^2} \qquad (10)$$

where $\hat{x}, \hat{y}, \hat{z}$ are the position components estimates. The attitude error is computed following [24]:

$$e_R = arccos\left(1 - \frac{tr(\mathbf{I} - \mathbf{A}^T\hat{\mathbf{A}})}{2}\right) \qquad (11)$$

with $\hat{\mathbf{A}}$ being the estimated rotation matrix. The results of the V-SLAM algorithm in terms of position and attitude reconstruction are presented in Fig. 5, considering both sensing modalities.
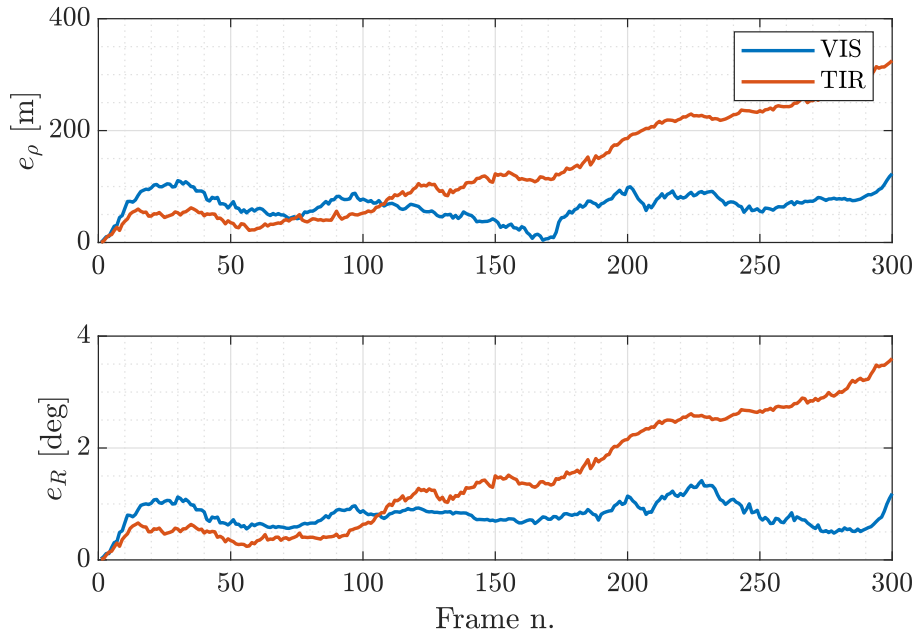

Figure 5: Position (top) and attitude (bottom) error, test case n.1

It can be noticed that the VIS sensing mode performs well on a long sequence, keeping the overall position error below 2.2 % of the range and the attitude one below 1.5°. Considering instead the TIR sensing mode, it is evident that the reduced sensor size negatively affects the pose estimation, with an overall position error that can reach up to 6.5 % of the range. The overall error reaches values that

7

are too high for practical applications, and accuracy should be enhanced either by adding a further optimization step (full BA) or by performing data fusion.

This long sequence is also useful to assess the shape reconstruction performances. The obtained sparse 3D maps are reported in Fig. 6. Please notice that the scale is arbitrary at this stage, and thus no units have been introduced. Mapping performances are indeed satisfactory in both cases, in fact the overall shape of the asteroid is well-reconstruced. Nevertheless, it is worth underlining the fact that the map reconstructed with the TIR sensing mode presents a slightly higher number of outlier points, and it is less uniform, while the VIS map is extremely homogeneous in terms of spatial distribution, thanks to ANMS-SSC feature point bucketing.

Figure 6: Asteroid shape reconstruction

(a) Shape reconstruction, VIS mode   **(b) Shape reconstruction, TIR mode**
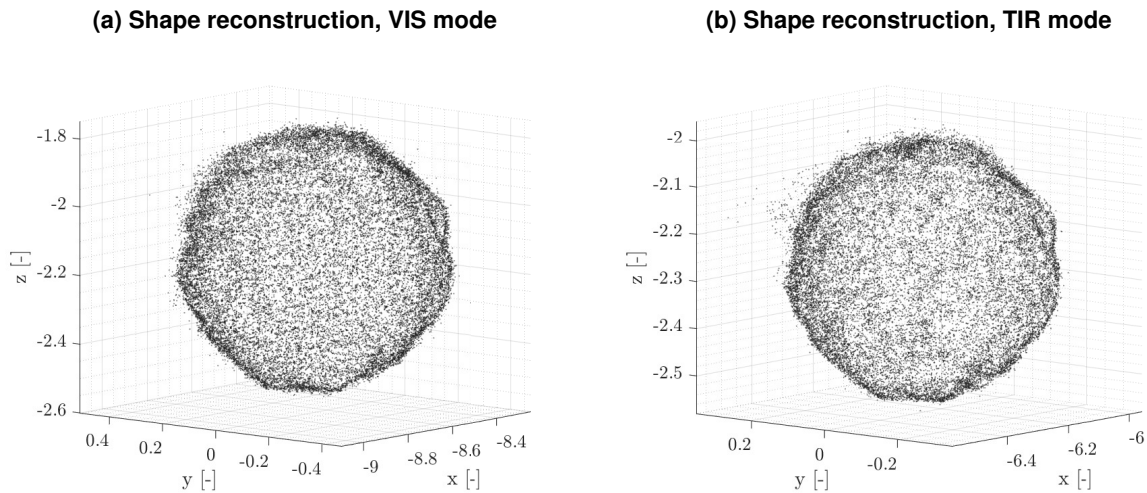
Once a 3D sparse map is available, a polyhedron model can be retrieved to further assess the validity of the reconstructed shape. The resulting triangulation for the VIS sparse 3D map, that is the best one, is presented in Fig. 7

Figure 7: Polyhedron shape model reconstruction

8
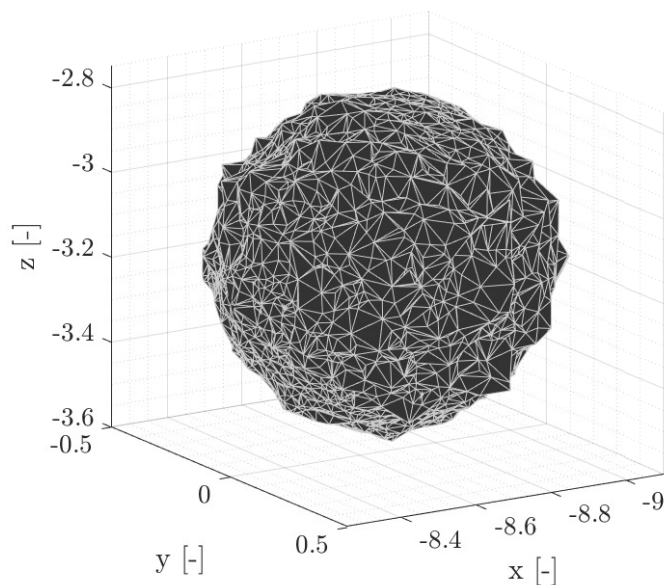
4. Filtering

To combine information coming from the VIS and TIR camera, a filtering procedure is performed. In this work, a coupled position-attitude filter is considered, that makes it possible to obtain observability of the asteroid's angular velocity.

4.1. Algorithm description

The Extended Kalman Filter is the most widespread filtering technique when dealing with nonlinear system estimation. The idea behind this method is quite straightforward. The non-linear system is linearized around the current state estimate, and the state update is performed using a small perturbation discrete linear model. Considering a generic non-linear system:

$$\begin{aligned} \dot{\mathbf{X}} &= f(\mathbf{X}, t) + \mathbf{G}(\mathbf{X})w \\ \mathbf{Y} &= h(\mathbf{X}, t) + v \end{aligned} \tag{12}$$

f is a non-linear function, w is a zero-mean, Gaussian process noise with known covariance $\mathbf{Q}$ and $\mathbf{G}$ is a noise mapping function. The system output is linked to the current state $\mathbf{X}$ by a non-linear function h, while v is a zero-mean, Gaussian process noise with known standard deviation.

Once the full non-linear model has been obtained, it is necessary to derive the linearized model to fully develop the EKF estimation algorithm. Defining $\delta\mathbf{X}$ as a small perturbation around the reference condition (i.e the current state estimate), the linear perturbation model can be written as:

$$\begin{aligned} \delta\dot{\mathbf{X}} &= F(\mathbf{X})\delta\mathbf{X} + Gw \\ \delta\mathbf{Y} &= H(\mathbf{X})\delta\mathbf{X} + v \end{aligned} \tag{13}$$

where $F(\mathbf{X})$ and $H(\mathbf{X})$ are the Jacobian matrices of $f(X)$ and $h(X)$ respectively. The last step towards the development of the EKF algorithm is the defition of the State-Transition-Matrix (STM), that is reported in Eq. (14):

$$\mathbf{\Phi}(t, t_0) = \frac{\partial f(t)}{\partial f(t_0)} \tag{14}$$

and it can be obtained integrating Eq. (15):

$$\mathbf{\Phi}(t, t_0) = \int_{t_0}^{t} \dot{\mathbf{\Phi}}(\tau, t_0)d\tau \tag{15}$$

where

$$\begin{cases} \mathbf{\Phi}(t, t_0) = F(t)\mathbf{\Phi}(t, t_0) \\ \mathbf{\Phi}(t, t_0) = I \end{cases} \tag{16}$$

The EKF routine is summarized in algorithm 1, in which $\mathbf{Q}$ is the process covariance matrix, while $\mathbf{R}$ is the measurement covariance matrix. The only exception to the traditional EKF scheme is the posterior covariance update, which is computed through the Joseph's Formula for stability reasons [25]

Algorithm 1 Extended Kalman Filter

1: $\hat{\mathbf{X}}_k^- = \int_{t_{k-1}}^{t_k} f(\mathbf{X}(\tau))d\tau, \qquad \hat{\mathbf{X}}_0 = \mathbf{X}_0, \qquad \mathbf{X}_{k-1} = \hat{\mathbf{X}}_{k-1}$
2: $\mathbf{P}_k^- = \mathbf{\Phi}(t_k, t_{k-1})\mathbf{P}_{k-1}^+ \mathbf{\Phi}^T(t_k, t_{k-1}) + \mathbf{GQG}^T \Delta t$
3: $\mathbf{K}_k = \mathbf{P}_k^- \mathbf{H}_k^T (\mathbf{H}_k \mathbf{P}_k^- \mathbf{H}_k^T + \mathbf{R}_k)^{-1}$
4: $\hat{\mathbf{X}}_k^+ = \hat{\mathbf{X}}_k^- + \mathbf{K}_k(\mathbf{Y}_k - h(\hat{\mathbf{X}}_k^-))$
5: $\mathbf{P}_k^+ = (\mathbf{I} - \mathbf{K}_k\mathbf{H}_k)\mathbf{P}_k^-(\mathbf{I} - \mathbf{K}_k\mathbf{H}_k)^T + \mathbf{K}_k\mathbf{R}\mathbf{K}_k^T$

A quaternion-based representation is then selected to parametrize the attitude states. However, this choice needs to be coupled with a dedicated filtering approach, in order to deal with the non-uniqueness of this formulation. Even though it is possible to use an additive quaternion error, this representation leads to ill-conditioning of the covariance matrix, and orthonormality of the attitude matrix is no longer guaranteed. To overcome these issues, a multiplicative quaternion error is adopted, which is the basic principle of the Multiplicative EKF (MEKF) [26]. The MEKF uses the quaternion as a global attitude representation and use a three-component state vector $\delta\theta$ for the local representation of attitude errors. The multiplicative approach also has the advantage of reducing the size of the state, and thus of the covariance matrix. The full derivation of the error state model is available in [26], while only the non-linear state model is here reported for brevity.

4.1.1. Reference frames

Three reference frames are used for the development of the navigation filter: asteroid inertial, asteroid fixed and body fixed, that are labeled as $\mathcal{I}$, $\mathcal{A}$ and $\mathcal{B}$ respectively. Asteroid inertial frame and asteroid fixed frame share the same origin (the centre of mass of the small body), with the latter being attached to the tumbling asteroid itself. The body fixed frame is instead attached to the spacecraft, and it is assumed to be coincident with the camera reference frame.

4.1.2. Dynamical propagation

The main goal of the navigation system is to estimate the relative position, velocity and attitude with respect to the asteroid frame. The asteroid's angular rate, which is unknown, acts as a coupling term for the relative translational and rotational dynamics, and thus it is included in the state vector. The probe's attitude kinematics with respect to the asteroid fixed frame is a function of both the asteroid's spin state and of the inertial angular velocity, which is measured by the gyroscope. Due to the fact that the gyroscope is susceptible to a drifting error, it is a common practice to include the gyroscope bias in the state vector, together with the inertial attitude state. The global state vector can be then defined as:

$$\mathbf{X} = \begin{bmatrix} \mathbf{r}_A & \mathbf{v}_A & \mathbf{q}_{B/A} & \mathbf{q}_{B/I} & \boldsymbol{\beta} & \boldsymbol{\omega}_{A/I} \end{bmatrix}^T \tag{17}$$

Where $(\mathbf{r}_A, \mathbf{v}_A)^T$ are the position and velocity vectors expressed in the asteroid fixed frame, $\mathbf{q}_{B/A}$ represents the spacecraft's relative attitude with respect to the asteroid fixed frame, $\mathbf{q}_{B/I}$ is the attitude with respect to the inertial frame, $\boldsymbol{\beta}$ is the gyroscope bias expressed in the body frame and $\omega_{A/I}$ is the asteroid's spin state with respect to the inertial frame. The usual Kalman filter update equations can be employed to include gyro data in the EKF as measurements. However, a great number of attitude filters incorporate gyro information as part of the dynamics instead of using the gyro information as a Kalman measurement update. This alternative is often referred to as *dynamic model replacement* mode. The adopted approach does not require a model of rotational dynamics and torques, which in turns avoids the modeling of the spacecraft's inertia and control action. Considering the asteroid's rotational dynamics, a constant angular velocity has been assumed. The complete derivation of the non-linear model is available in [27], while only the final expression is here reported for conciseness, considering the notation of Eq. (12).

$$f(\mathbf{X}) = \begin{cases} \mathbf{v}_A \\ -\dfrac{\mu}{r_A^3}\mathbf{r}_A - 2\omega_{A/I} \times \mathbf{v}_A - \omega_{A/I} \times (\omega_{A/I} \times \mathbf{r}_A) \\ \dfrac{1}{2}\Omega\big(\tilde{\omega}_{B/I} - \boldsymbol{\beta} - \mathbf{A}_{B/A}\omega_{A/I}\big)\mathbf{q}_{B/A} \\ \dfrac{1}{2}\Omega\big(\tilde{\omega}_{B/I} - \boldsymbol{\beta}\big)\mathbf{q}_{B/I} \\ \mathbf{0} \\ \mathbf{0} \end{cases} \tag{18}$$

Where $A_{B/A}$ is the attitude matrix $A(q_{B/A})$ that links the body fixed frame to the asteroid fixed frame and $\tilde{\omega}$ is the measured angular rate. The expression $\boldsymbol{\Omega}(\mathbf{v})$ reads:

$$\Omega(\omega) = \begin{bmatrix} 0 & v_z & -v_y & v_x \\ -v_z & 0 & v_x & v_y \\ v_y & -v_x & 0 & v_z \\ -v_x & -v_y & -v_z & 0 \end{bmatrix} \tag{19}$$

being $\mathbf{v}$ a generic 3-component vector.

The noise mapping matrix $\mathbf{G}$ and the process noise vector $\mathbf{w}$ complete the non-linear propagation:

$$G(\mathbf{X}) = \begin{bmatrix} \mathbf{0}_{3\times3} & \mathbf{0}_{3\times3} & \mathbf{0}_{3\times3} & \mathbf{0}_{3\times3} \\ \mathbf{I}_{3\times3} & \mathbf{0}_{3\times3} & \mathbf{0}_{3\times3} & \mathbf{0}_{3\times3} \\ \mathbf{0}_{4\times3} & \frac{1}{2}\Xi(\mathbf{q}_{B/A}) & \mathbf{0}_{4\times3} & \mathbf{0}_{4\times3} \\ \mathbf{0}_{4\times3} & \frac{1}{2}\Xi(\mathbf{q}_{B/I}) & \mathbf{0}_{4\times3} & \mathbf{0}_{4\times3} \\ \mathbf{0}_{3\times3} & \mathbf{0}_{3\times3} & \mathbf{0}_{3\times3} & \mathbf{I}_{3\times3} \end{bmatrix} \qquad w = \begin{pmatrix} \boldsymbol{\eta}_g \\ \boldsymbol{\eta}_v \\ \boldsymbol{\eta}_u \\ \boldsymbol{\eta}_\omega \end{pmatrix} \tag{20}$$

In which $\Xi(\mathbf{q})$ is defined as:

$$\Xi(\mathbf{q}) = \begin{bmatrix} q_4 \mathbf{I}_3 - [\mathbf{q}_{1:3}\times] \\ -\mathbf{q}_{1:3}^T \end{bmatrix} \tag{21}$$

Considering the process noise components, $\boldsymbol{\eta}_g$ is an artificial white noise ($\boldsymbol{\eta}_g \sim \nu(0, \boldsymbol{\sigma}_g)$), whose aim is to compensate for the errors in the gravity field model introduced by the keplerian motion simplification. The noise vectors $\boldsymbol{\eta}_v$ and $\boldsymbol{\eta}_u$ are instead linked to the gyroscope characteristics. Lastly, an artificial white noise $\boldsymbol{\eta}_\omega$ is added to the asteroid rotational dynamics to ease the estimation process.

4.1.3. Measurement model

To perform the EKF update, the filter must process information coming from the available sensors. In spite of the fact that the VIS and TIR navigation cameras represent the most important source of information, their contribution must be fused with inertial measurements reconstruct the whole state vector. Besides gyroscope measurements, that have already been discussed, it is assumed that a star tracker and an altimeter are available onboard.

Star Tracker. The star tracker provides information regarding the inertial attitude of the probe. For simplicity, the instrument is supposed to have direct quaternion-out capabilities, therefore a noisy quaternion is readily available:

$$\mathbf{Y}_{star} = \boldsymbol{q}_{star} = \tilde{\boldsymbol{q}}_{B/I} \tag{22}$$

Altimeter. The ranging measurement provides the magnitude of the relative distance to the asteroid:

$$\mathbf{Y}_\varrho = \varrho = \|\mathbf{r}_A\| \tag{23}$$

Camera. Considering the implemented V-SLAM pipeline, direct pose measurements are available:

$$\mathbf{Y}_{cam} = \begin{bmatrix} \mathbf{r}_A \\ \boldsymbol{q}_{B/A} \end{bmatrix} \tag{24}$$

The full measurement vector is thus:

$$\mathbf{Y}_k = \begin{bmatrix} \varrho & \boldsymbol{q}_{B/I} & \mathbf{r}_A & \boldsymbol{q}_{B/A} \end{bmatrix}^T \tag{25}$$

Notice that in this case only range measurements require the actual computation of the Jacobian matrix $\mathbf{H}_\varrho$, while all the other quantities are linearly related to the state vector.

4.1.4. Measurement check

Due to the presence of outliers in the measurements, not all the data delivered by the IP should actually be processed by the filter. It is then necessary to implement an outlier-rejection strategy nested within the filtering scheme, to make it robust to IP faults and errors. To detect the presence of outliers in the observations, that are theoretically Gaussian distributed, the so called *null-hypothesis* test is performed, similarly to [28]. Since it is assumed that observations are Gaussian, with known mean and standard deviation, in case there are some outliers, the normal probability density function does not hold anymore. The aim of the null-hypothesis test is to check whether the actual measurement is compatible with the assumed model, i.e null-hypothesis. As highlighted in [29], the judging index can be set to the square of the Mahalanobis distance:

$$\gamma_k = M_k^2 = (\mathbf{Y}_k - h(\mathbf{X}_k^-))^T (\mathbf{P}_{y_k})^{-1} (\mathbf{Y}_k - h(\mathbf{X}_k^-)) \tag{26}$$

where

$$\mathbf{P}_{y_k} = \mathbf{H}_k \mathbf{P}_k^- \mathbf{H}_k^T + \mathbf{R}_k \tag{27}$$

Assuming that the null-hypothesis is true, γ_k should be Chi-square distributed with degree of freedom m. A significance level α, that is a probability threshold below which the null hypothesis will be rejected, is selected. α is typically a small number, which is here set to $\alpha = 0.05$. Please notice that the α-quantile χ_α of the Chi-square distribution is predetermined for a given threshold α and number of degrees of freedom m. It is then possible to write:

$$\mathcal{P}(\gamma_k > \chi_\alpha) = \alpha \tag{28}$$

which implies that the probability of a randomly selected γ_k (still to be evaluated for the actual measurement $\mathbf{Y}_k$) being greater than χ_α should be equal to α. The performance index γ_k is then evaluated for the available measurement, and the test is performed. If it occurs that $\gamma_k > \chi_\alpha$ the null hypothesis is rejected, and it can be concluded that the current observation is actually an outlier.

4.2. Simulation scenario

4.2.1. Reference dynamical model

In order to validate and assess the performance of the filter, a preliminary test campaign has been performed separately with respect to the V-SLAM pipeline. An hyperbolic arc has been selected for the probe, with eccentricity of 1.2 and pericenter radius of 5km. A duration of 5.5 hours is considered for the simulation. The main attractor's shape is roughly known from ground observation, and an high fidelity model has been developed and used in several researches, according to the gravity field expression from a polyhedral object [30], whose physical properties are taken from [13]. Concerning the rotational dynamics of the asteroid, it has been assumed to be mainly rotating about its $z-$axis. A small deviation is then introduced to reproduce the highly perturbed dynamics of such objects:

$$\boldsymbol{\omega}_{A/I} = \begin{bmatrix} cos(\delta\lambda)sin(\delta\theta) \\ sin(\delta\lambda)sin(\delta\theta) \\ cos(\delta\theta) \end{bmatrix} \omega_z \tag{29}$$

Where $\delta\theta$ is a generic perturbation, with $\delta\theta = 0$ corresponding to the reference state. The rotational axis draws a cone about the z_A axis, experiencing precession. In this work $\delta\theta = \delta\lambda = 3°$ is considered.

For the probe's rotational dynamics, a nadir-pointing attitude guidance is imposed, in such way that the camera's boresight, that coincides with the $z-$axis of the body fixed frame, always points towards the asteroid's center of mass. To satisfy the pointing constraint, the spacecraft must rotate around its y-axis, that is aligned with the orbital angular momentum, at a rate given by:

$$\boldsymbol{\omega}_{B/I} = \begin{bmatrix} 0 & h/\varrho^2 & 0 \end{bmatrix}^T \tag{30}$$

Where h is the orbital angular momentum and ϱ is the distance from the primary body.

4.2.2. Hardware model

The gyroscope is usually sampled at a high rate, therefore a discrete model is sufficient for this simulations' purposes. Artificial noise is introduced in terms of a random constant and a random walk. The discrete time model provided by *Markley* and *Crassidis* [26] is here adopted.

$$\tilde{\boldsymbol{\omega}}_{k+1} = \boldsymbol{\omega}_k + \frac{1}{2}(\boldsymbol{\beta}_{k+1} + \boldsymbol{\beta}_k) + \left(\frac{\sigma_v^2}{\Delta t} + \frac{1}{12}\sigma_u^2\Delta t \right)^{1/2} \boldsymbol{\eta}_v \tag{31}$$

$$\boldsymbol{\beta}_{k+1} = \boldsymbol{\beta}_k + \sigma_u\Delta t^{1/2}\boldsymbol{\eta}_u \tag{32}$$

where the subscript k denotes the $k-th$ time step, while $\boldsymbol{\eta}_v$ and $\boldsymbol{\eta}_u$ are zero-mean Gaussian white-noise processes with known variance σ_v and σ_u. The gyroscope considered in this work is the AIRBUS-Astrix 120 [31]. The star tracker output $\tilde{\mathbf{q}}_{B/I}$ is obtained perturbing the nominal quaternion with a small measurement noise quaternion $\delta\mathbf{q}_n$.

$$\tilde{\mathbf{q}}_{B/I} = \delta\mathbf{q}_n^{-1}\mathbf{q}_{B/I} \tag{33}$$

Typical accuracy values and update rate have been taken from the datasheet of AA-STR tracker by Leonardo [32], on-board the ongoing ESA mission Bepi-Colombo. It is worth underlying that a higher error is attributed to the measurements along the instrument's boresight axis, which in this case is aligned with the Y-axis of the body-fixed frame.

Considering now the navigation cameras output, measurements have been generated artificially, considering the performances highlighted in section 3. Position measurements were obtained corrupting the ground-truth trajectory with white Gaussian noise, while attitude measurements were computed through noisy quaternions, as previously done in Eq. (33) for the star tracker output. Outliers have been added to the measurements for realism purposes. For consistency, the camera update rate is the same as the one considered during the IP tests, while the other sensors update rates comply with real hardware capabilities and they are reported in Table 2. The propagation time step of the filter is set to 1s.

Table 2: Hardware sampling time

	Star Tracker	Altimeter	Gyroscope	Camera
Update rate [s]	1.00	1.00	1.00	30

4.3. Results

In this section, the results of the state determination are presented. A Montecarlo simulation of 250 runs is performed, considering the same set of measurements and uncertain initial conditions. The filter settings are reported in Table 3 and Table 4. Each submatrix of the covariance matrix is assumed to be isotropic. The initial state estimate is obtained by randomly sampling within the 3σ bounds of the initial covariance matrix.

Table 3: Process noise settings

Parameter	Value	Unit
σ_g	5.00e-07	km/s^2
σ_v	2.74e-07	$rad/s^{1/2}$
σ_u	2.24e-08	$rad/s^{3/2}$
σ_ω	8.00e-09	rad/s

Table 4: Initial covariance settings

Parameter	Value	Unit
$\mathbf{P}_0, r_A$	$[3e-02]^2$	km^2
$\mathbf{P}_0, v_A$	$[3e-03]^2$	km^2/s^2
$\mathbf{P}_0, q_{B/A}$	$[3e-03]^2$	-
$\mathbf{P}_0, q_{B/I}$	$[3e-05]^2$	-
$\mathbf{P}_0, \beta$	$[1e-06]^2$	rad^2/s^2
$\mathbf{P}_0, \omega_{A/I}$	$[1e-06]^2$	rad^2/s^2

Position and attitude errors are computed as in Eq. (10) and Eq. (11) respectively, while the angular velocity estimation error reads:

$$e_\omega = \sqrt{(\omega_{x,i} - \hat{\omega}_{x,i})^2 + (\omega_{y,i} - \hat{\omega}_{y,i})^2 + (\omega_{z,i} - \hat{\omega}_{z,i})^2} \tag{34}$$

Position, relative attitude and spin state estimation error is shown in Fig. 8, considering all three sensing modalities.

Figure 8: Position (top), relative attitude (middle) and asteroid's spin (bottom) estimation error
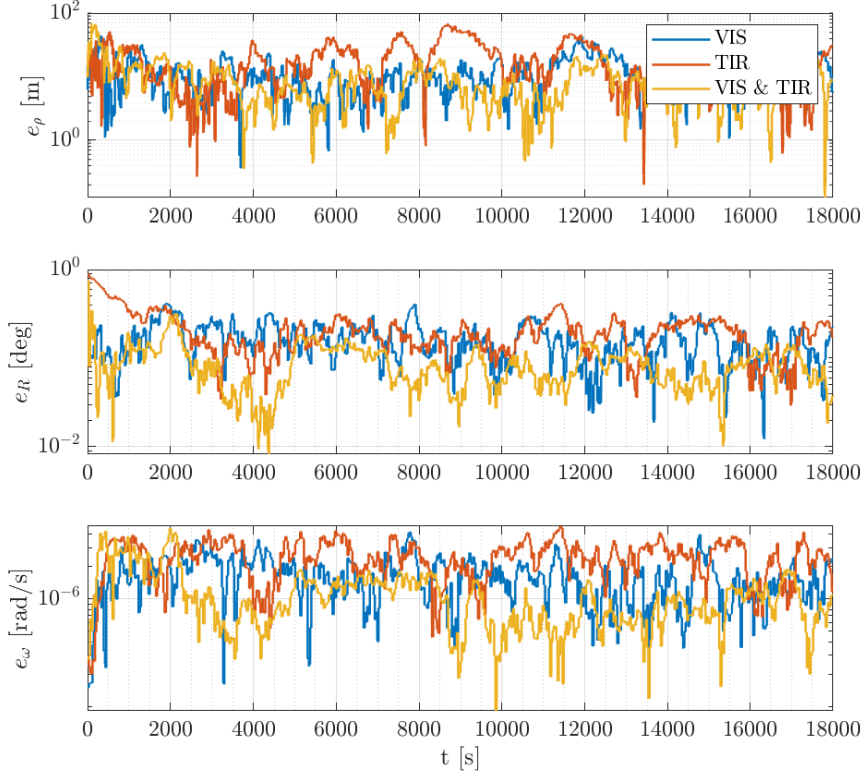
Although TIR images offer reduced performances with respect to VIS data, the adopted approach highlights that the VIS-TIR measurements fusion leads to improvements in the order of 25%, 22% and 11% in localization, attitude and spin state estimation respectively, compared to VIS camera exploitation

only. It is also worth noticing the fact that spin state estimation improvement linked to data fusion is not as evident as in the case of the relative pose, since it is only recovered through the state dynamical model and not by means of direct measurements. A comprehensive performance summary of the Montecarlo simulations is reported in Table 5, including the mean computational time.

Table 5: Estimation RMSE and run time

	ϱ_A [m]	$\dot{\varrho}_A$ [m/s]	$\mathbf{A}_{B/A}$ [deg]	$\mathbf{A}_{B/I}$ [deg]	β [rad/s]	$\omega_{A/I}$ [rad/s]	Time [s]
VIS	11.823	0.032	0.108	3.237e-03	7.936e-07	4.462e-07	28.0854
TIR	17.265	0.029	0.127	3.069e-03	7.917e-07	4.808e-07	28.0731
VIS & TIR	8.885	0.030	0.084	3.174e-03	7.941e-07	4.121e-07	28.4203

As expected, since star tracker measurements are not related to camera ones, the gyroscope bias and inertial attitude estimation errors do not change according to the selected modality. Analyzing the computational load associated to each sensing modality, it can be concluded that only a modest 1% increase occurs when both VIS and TIR camera output is processed by the filter. This computational load is mainly due to the evaluation of the Mahalanobis distance, since it involves matrix inversion operations.

5. Conclusion

This paper investigates the possibility of combining visible and thermal infrared imagery for relative navigation and mapping of small celestial bodies. The presented analyses show that despite the reduced resolution of TIR imagers, classical feature-based navigation algorithms can still produce meaningful results. Given the promising results obtained on synthetically generated images, further studies will be carried out exploiting the experimental facility at Politecnico di Milano Department of Aerospace Science and Technologies. The developed filtering scheme is a clear advantage for the relative state estimation. Furthermore, the combination of the inertial and relative attitude dynamics makes it possible to include the asteroid's angular velocity in the state vector. Results highlight that TIR-based measurements can improve both the accuracy and the robustness of the state estimation algorithm. Again, a more extensive analysis needed for the filtering block to assess its performances when dealing with direct IP measurements.

References

[1] P. Michel, C. Reed, I. Carnelli, A. Gálvez, S. Ulamec, A. the, Aida: Asteroid impact and deflection assessment mission under study at esa and nasa, in: Conference on Spacecraft Reconnaissance of Asteroid and Comet Interiors, 2015, pp. 1–5.

[2] R. Gaskell, O. Barnouin-Jha, D. J. Scheeres, A. Konopliv, T. Mukai, S. Abe, J. Saito, M. Ishiguro, T. Kubota, T. Hashimoto, et al., Characterizing and navigating small bodies with imaging data, Meteoritics & Planetary Science 43 (6) (2008) 1049–1061.

[3] M. Piccinin, M. R. Lavagna, Deep reinforcement learning approach for small bodies shape reconstruction enhancement, in: AIAA Scitech 2020 Forum. `doi:10.2514/6.2020-1909`.

[4] T. Okada, M. Taguchi, S. Tanaka, N. Sakatani, K. Suko, Y. Ogawa, T. Sekiguchi, T. Kouyama, J. Helbert, T. Müller, A. Hagermann, J. Biele, M. Grott, M. Hamm, M. Delbo, Thermal inertia of asteroid ryugu using dawn-side thermal images by tir on hayabusa2, 2019.

[5] D. A. Lorenz, R. Olds, A. May, C. Mario, M. E. Perry, E. E. Palmer, M. Daly, Lessons learned from osiris-rex autonomous navigation using natural feature tracking, in: 2017 IEEE Aerospace Conference, 2017, pp. 1–12. `doi:10.1109/AERO.2017.7943684`.

[6] N. Ogawa, F. Terui, S. Yasuda, K. Matsushima, T. Masuda, J. Sano, H. Hihara, T. Matsuhisa, S. Danno, M. Yamada, Y. Mimasu, K. Yoshikawa, G. Ono, Y. Yokota, T. Saiki, Y. Tsuda, Image-based Autonomous Navigation of Hayabusa2 using Artificial Landmarks: Design and In-Flight Results in Landing Operations on Asteroid Ryugu. `doi:10.2514/6.2020-0225`.

[7] T. Okada, Thermography of asteroid and future applications in space missions, Applied Sciences 10 (6) (2020) 2158. `doi:https://doi.org/10.3390/app10062158`.

[8] STAR-Dundee, Planet and asteroid natural scene generation utility (2019).
URL `https://pangu.software/`

[9] A. Harris, J. Lagerros, Asteroids in the Thermal Infrared, 2002, pp. 205–218.

[10] I. Pelivan, L. Drube, E. Kührt, J. Helbert, J. Biele, M. Maibaum, B. Cozzoni, V. Lommatsch, Thermophysical modeling of didymos' moon for the asteroid impact mission, Advances in Space Research 59 (7) (2017) 1936 – 1949. `doi:https://doi.org/10.1016/j.asr.2016.12.041`.

[11] M. Delbo, M. Mueller, J. P. Emery, B. Rozitis, M. T. Capria, Asteroid thermophysical modeling, Asteroids IV (2015). `doi:10.2458/azu_uapress_9780816532131-ch006`.

[12] B. Burmann, I. Gerth, M. Scheper, M. Lavagna, F. Ferrari, J. Vasconcelos, J. Seabra, Close-proximity operations concept of the asteroid impact mission, in: 67th International Astronautical Congress (IAC 2016), International Astronautical Federation, IAF, Beijing, China, 2016.

[13] AIM, Asteroid impact mission: Didymos reference model, reference document v3.1, ESA (2015).

[14] B. Triggs, P. F. McLauchlan, R. I. Hartley, A. W. Fitzgibbon, Bundle adjustment — a modern synthesis, in: B. Triggs, A. Zisserman, R. Szeliski (Eds.), Vision Algorithms: Theory and Practice, 2000, pp. 298–372.

[15] E. Rublee, V. Rabaud, K. Konolige, G. Bradski, Orb: An efficient alternative to sift or surf, in: 2011 International Conference on Computer Vision, 2011, pp. 2564–2571. `doi:10.1109/ICCV.2011.6126544`.

[16] H. Bay, A. Ess, T. Tuytelaars, L. Van Gool, Speeded-up robust features (surf), Computer Vision and Image Understanding 110 (3) (2008) 346 − 359, similarity Matching in Computer Vision and Multimedia. `doi:https://doi.org/10.1016/j.cviu.2007.09.014`.

[17] O. Bailo, F. Rameau, K. Joo, J. Park, O. Bogdan, I. S. Kweon, Efficient adaptive non-maximal suppression algorithms for homogeneous spatial keypoint distribution, Pattern Recognition Letters 106 (2018) 53 − 60. `doi:https://doi.org/10.1016/j.patrec.2018.02.020`.

[18] J.-Y. Bouguet, et al., Pyramidal implementation of the affine lucas kanade feature tracker description of the algorithm, Intel corporation 5 (1-10) (2001) 4.

[19] D. Nister, An efficient solution to the five-point relative pose problem, IEEE Transactions on Pattern Analysis and Machine Intelligence 26 (6) (2004) 756–770.

[20] P. Torr, A. Zisserman, Mlesac: A new robust estimator with application to estimating image geometry, Computer Vision and Image Understanding 78 (1) (2000) 138 − 156.

[21] Xiao-Shan Gao, Xiao-Rong Hou, Jianliang Tang, Hang-Fei Cheng, Complete solution classification for the perspective-three-point problem, IEEE Transactions on Pattern Analysis and Machine Intelligence 25 (8) (2003) 930–943.

[22] V. Lepetit, F. Moreno-Noguer, P. Fua, Epnp: An accurate o(n) solution to the pnp problem, International Journal Of Computer Vision 81 (2009) 155–166.

[23] M. I. A. Lourakis, A. A. Argyros, Sba: A software package for generic sparse bundle adjustment, ACM Trans. Math. Softw. 36 (1) (Mar. 2009). `doi:10.1145/1486525.1486527`.

[24] L. Markley, D. Mortari, Quaternion attitude estimation using vector observations, Journal of the Astronautical Sciences 48 (04 2000). `doi:10.1007/BF03546284`.

[25] J. R. Carpenter, C. N. D. Souza, Navigation filter best practices, Technical report, NASA (2018).

[26] F. L. Markley, J. L. Crassidis, Fundamentals of spacecraft attitude determination and control, Space Technology Library, Springer, New York, NY, 2014. `doi:10.1007/978-1-4939-0802-8`.

[27] G. L. Civardi, Multispectral vision-based navigation and spin state estimation for unknown and uncooperative space objects, Master's thesis, Politecnico di Milano (2021).

[28] S. Silvestrini, A. Capannolo, M. Piccinin, M. R. Lavagna, J. G. Fernandez, Centralized autonomous relative navigation of multiple spacecraft around small bodies, in: AIAA Scitech 2020 Forum. `doi:10.2514/6.2020-1204`.

[29] G. Chang, Robust Kalman filtering based on Mahalanobis distance as outlier judging criterion, Journal of Geodesy 88 (4) (2014) 391–401. `doi:10.1007/s00190-013-0690-8`.

[30] R. A. Werner, D. J. Scheeres, Exterior gravitation of a polyhedron derived and compared with harmonic and mascon gravitation representations of asteroid 4769 castalia, Celestial Mechanics and Dynamical Astronomy 65 (1996).

[31] AIRBUS, Astrix-120 (2020).
URL `https://www.airbus.com/space/spacecraft-equipment/avionics/astrix.html`

[32] Leonardo, Aa-str star tracker (2020).
URL `https://www.leonardocompany.com/en/products/aastr`